

Journal of Astronomical Telescopes, Instruments, and Systems

AstronomicalTelescopes.SPIEDigitalLibrary.org

Observational artifacts of Nuclear Spectroscopic Telescope Array: ghost rays and stray light

Kristin K. Madsen
Finn E. Christensen
William W. Craig
Karl W. Forster
Brian W. Grefenstette
Fiona A. Harrison
Hiromasa Miyasaka
Vikram Rana

SPIE.

Kristin K. Madsen, Finn E. Christensen, William W. Craig, Karl W. Forster, Brian W. Grefenstette, Fiona A. Harrison, Hiromasa Miyasaka, Vikram Rana, "Observational artifacts of Nuclear Spectroscopic Telescope Array: ghost rays and stray light," *J. Astron. Telesc. Instrum. Syst.* **3**(4), 044003 (2017), doi: 10.1117/1.JATIS.3.4.044003.

Observational artifacts of Nuclear Spectroscopic Telescope Array: ghost rays and stray light

Kristin K. Madsen,^{a,*} Finn E. Christensen,^b William W. Craig,^c Karl W. Forster,^a Brian W. Grefenstette,^a Fiona A. Harrison,^a Hiromasa Miyasaka,^a and Vikram Rana^a

^aCalifornia Institute of Technology, Space Radiation Laboratory, Pasadena, California, United States

^bTechnical University of Denmark, National Space Institute, Lyngby, Denmark

^cUniversity of California, Space Sciences Laboratory, Berkeley, California, United States

Abstract. The Nuclear Spectroscopic Telescope Array (NuSTAR) launched in June 2012, flies two conical approximation Wolter-I mirrors at the end of a 10.15-m mast. The optics are coated with multilayers of Pt/C and W/Si that operate from 3 to 80 keV. Since the optical path is not shrouded, aperture stops are used to limit the field of view (FoV) from background and sources outside the FoV. However, there is still a sliver of sky (~1.0 deg to 4.0 deg) where photons may bypass the optics altogether and fall directly on the detector array. We term these photons stray light. Additionally, there are also photons that do not undergo the focused double reflections in the optics, and we term these ghost rays. We present detailed analysis and characterization of these two components and discuss how they impact observations. Finally, we discuss how they could have been prevented and should be in future observatories. © The Authors. Published by SPIE under a Creative Commons Attribution 3.0 Unported License. Distribution or reproduction of this work in whole or in part requires full attribution of the original publication, including its DOI. [DOI: 10.1117/1.JATIS.3.4.044003]

Keywords: Nuclear Spectroscopic Telescope Array; optics; satellite.

Paper 17029P received Jun. 27, 2017; accepted for publication Oct. 3, 2017; published online Oct. 27, 2017.

1 Introduction

The Nuclear Spectroscopic Telescope Array (NuSTAR), launched in June 2012,¹ is a focusing x-ray observatory operating in the energy range of 3 to 80 keV. The schematic of NuSTAR is shown in Fig. 1(a). It carries two coaligned conical Wolter-I approximation² optic modules that focus onto two identical focal plane modules (FPMs) called FPMA and FPMB. The optical and focal plane benches are separated by a mast providing a focal length of 10.15 m. A laser metrology system is used to keep track of the lateral and angular displacement of the two benches,³ which is caused by thermal motions in the mast, and a star tracker coaligned with the optics provides the absolute aspect.⁴ NuSTAR is a pointed observatory and averages about one observation a day.

In a regular Wolter-I geometry,^{5,6} the primary mirror is a paraboloid and the secondary a hyperboloid. In a Wolter-I approximation, the two surfaces have been replaced with conical sections that reduces the complexity of the build, but this comes at a cost of a larger point spread function (PSF). Both constructions allow for very shallow grazing incidence angles that improve the efficiency of reflection for reasonable focal lengths. One single mirror, however, presents a very small area, and to achieve a greater area multiple mirrors are typically nested, as shown in Fig. 2. The spacing of the shells impacts the geometrical area; a looser filling factor utilizes more of the geometrical area, but the extra spacing makes it possible for photons that only undergo one reflection, or none at all, to make it through to the focal plane, while a denser filling reduces this amount of nonfocused reflections but also reduces the area due to self shadowing of the shells. The NuSTAR design favors

a denser shell packing to reduce the nonfocused reflections, but not all of them can be completely eliminated.

Over the course of the first four years of operation, we have acquired very good knowledge of these nonfocused optical artifacts, which we collectively term ghost rays (GR); we present in Sec. 3 the analysis of their character. We compare the observations with raytrace simulations and confirm that we understand the source of the artifacts.

Because of the penetrating hard x-rays, it is not feasible to shroud the optical path, and, due to the open geometry, NuSTAR is susceptible to stray light (SL). The SL enters the detector aperture without having passed through the optics and undergone reflection. This component acts as an additional background⁷ and has implications for observatory planning. We present in Sec. 4 detailed characterization of the component and its mitigation.

In Sec. 5, we summarize our findings and discuss how these artifacts could have been avoided altogether and how they should be avoided in future observatories.

2 Detailed Instrument Overview

The two NuSTAR optics were built to be geometrically identical. The length of each conical mirror section is 227 mm, and the inner radius of the optics, where the two sections intersect, is 54.4 mm and the outer is 191.2 mm. To achieve a high geometric area, NuSTAR has 133 nested shells; the outer 43 shells are coated with a W/Si multilayer, whereas the inner 90 shells are coated with Pt/C, limiting the highest efficient reflective x-ray energy to the Pt 78.4 keV K-edge. A multilayer is a stack of two alternating material pairs, called a bilayer, and, in the case of NuSTAR, the bilayer thicknesses are graded with thicker layers at the top for low-energy reflection and thinner layers at the bottom for the high-energy reflection.^{8,9} The

*Address all correspondence to: Kristin K. Madsen, E-mail: kkm@caltech.edu

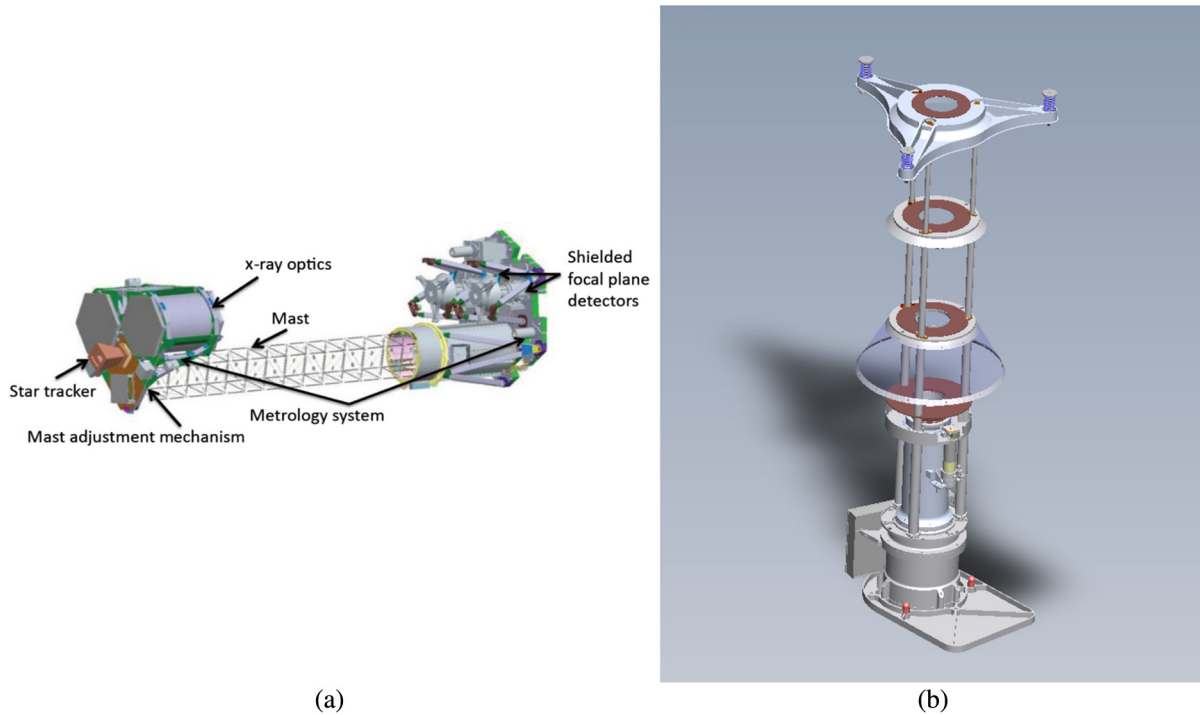


Fig. 1 (a) Schematic of NuSTAR. The dimension of the mast is not to scale. (b) Schematic of the focal plane and the aperture stop assembly.

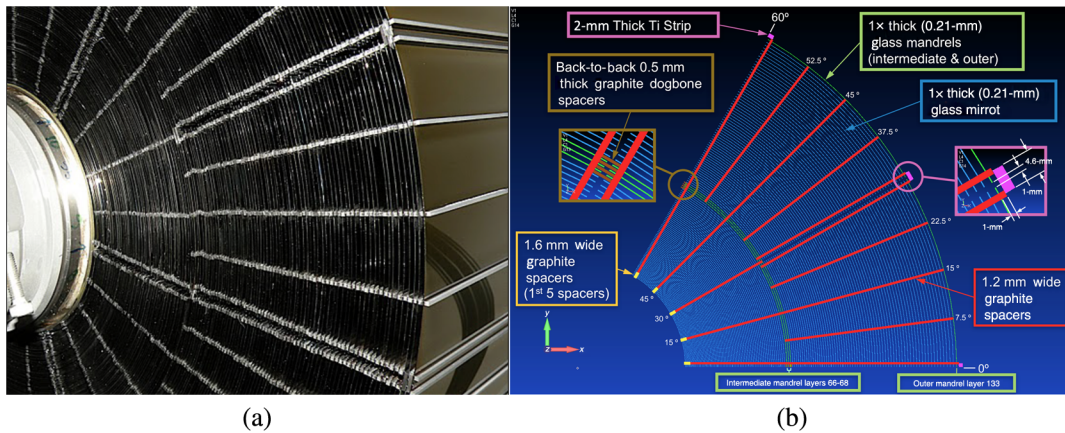


Fig. 2 (a) Photo of a NuSTAR optic showing the structure of the mirror module and the graphite spacers holding the layers together. (b) Schematic of the 60-deg wedge of the optics. The double “street” of spacers every 30 deg bounds a gap with no glass. This is the entry point of the “streak” discussed in Sec. 3.2. The support spiders, not shown here, obscure every other one of these gaps.

angle of the innermost shell with respect to the optical axis (OA) is $\alpha_{\text{primary,shell}=1} = 1.342 \text{ mrad}$ ($4.6'$) and $\alpha_{p,133} = 4.715 \text{ mrad}$ ($26.3'$) for the outermost shell. The angle of the secondary mirror is related to the primary by $\alpha_s = 3\alpha_p$.

A section of the optics and its schematic are shown in Fig. 2(b). The optics are segmented, and each shell is composed of multiple mirrors, mounted and held together by epoxied graphite spacers. The module can be divided into an inner and outer shell section that is separated by an intermediate mandrel, which is a strong-backed block of three shells (shells 66 to 68).¹⁰ For the inner shells (1 to 65), there are 12 mirror segments and the spacers are positioned every 15 deg, while for the outer shells (69 to 133) there are 24 segments and the spacers are positioned

every 12.5 deg. The span of the mirrors is also different between the inner and outer shells with 60 deg for the inner and 30 deg for the outer.

The graphite spacers appear as dark absorption elements in the PSF (for example, see Fig. 8). The gaps between mirror sections also appear as dark areas because there is no mirror to reflect the photons. For specific angles, however, as discussed in Sec. 3.2, these light up with x-rays that arrive unobstructed at the focal plane. A support spider, which holds the optics in place within their cans, blocks out the mirror gaps every 60 deg and completely eliminates the mirror gaps of the inner shells.

Three aperture stops are attached to each FPM as shown in Fig. 1(b). The top limiting aperture is located 833 mm from the

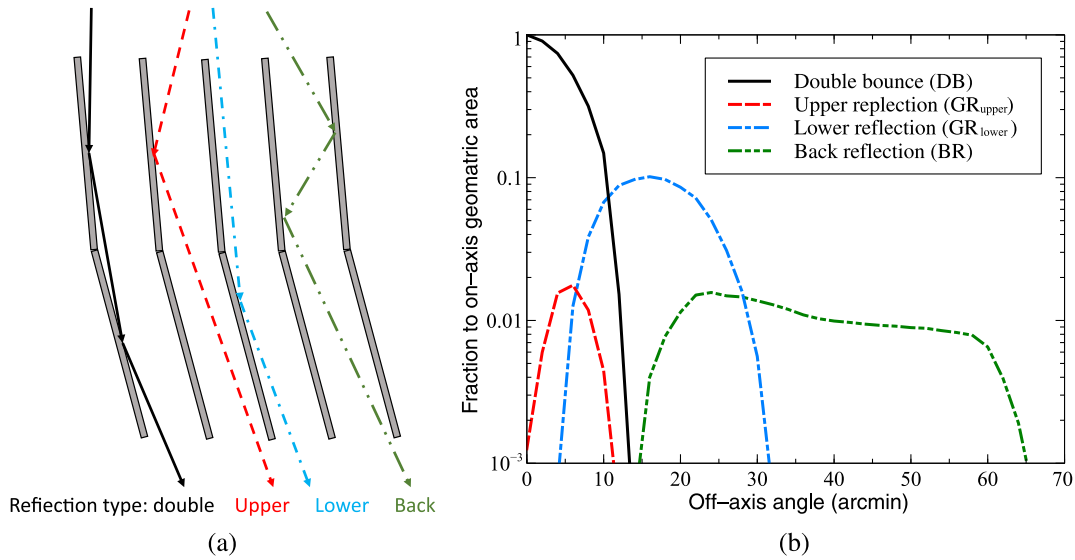


Fig. 3 (a) Illustration of different types of reflection in the optics. Black (solid) is the nominal double bounced reflection, which focuses the photons onto the focal plane. Red (dashed) and blue (dashed-dotted) are single reflections of the upper and lower conical mirror sections, respectively, collectively termed GR. The green (dashed-dotted-dotted) ray illustrates the BR situation where a photon strikes the backside of the adjacent mirror, then reflects off the front side of the upper section, and exits the optics. (b) The relative geometric area (not including reflectivity) of the various components in NuSTAR with respect to the on-axis geometric area. The areas have been corrected for aperture stop and the finite detector size.

surface of the detectors and has a diameter of 58 mm. The total thickness of the solid part of the aperture is designed to be 1.88 mm, layered into 0.75 mm Al, 0.13 mm Cu, and 1.0 mm Sn. These apertures act to limit the x-ray background and the SL from nearby sources.

The field of view (FoV) is determined by the detector, which has dimensions 40×40 mm and results in an FoV of $13.5 \times 13.5'$. The physical pixel size is $604.8 \mu\text{m}$ ($12.3''$), and a factor of five subpixel resolution is obtained in software for events sharing charge among multiple pixels to produce an effective pixel size of $2.5''$.

3 Ghost Rays

GR is the term given to the photons that only undergo a single reflection inside the optics. They either reflect from the upper (primary) or the lower (secondary) mirror section as shown in Fig. 3(a). In addition, there is a back reflected (BR) component in which the photons strike the backside of the adjacent mirror first before reflecting off the upper mirror.

The geometric area of all components, excluding the effects of reflection but including the aperture stop and the finite detector size, is shown in Fig. 3(b). The upper GR is the first component, and it is generated by photons that strike the upper mirrors at angles steeper than the nominal focusing graze angle. It dies out when the angle becomes so steep that the adjacent shell shadows it. The lower GR are made by photons arriving at angles that are shallower than the nominal graze angle. The lower GR reflections are thus produced on the opposite side of the mirror module than the upper GR as shown in Fig. 4. This figure also demonstrates that the aperture stop is responsible for limiting the upper GR component. The lower GR component dies out when the photon angle becomes equivalent to the angle of the mirror. At this point, the reflection of the

backside takes over. Because the shells have different angles, the components overlap. The true effective area, which includes the reflection, drastically alters the areas for all components as a function of energy.

Figure 5 shows raytraces of the GR component (a) at several different off-axis angles as they would appear on the detector, and a composite image of the GR (b) with and without the rejection of the aperture stop. This composite image does not include the BR component, and the fan feature extending from 20 – $60'$ in the upper image consists of photons that, if not for the aperture stop, would have made it straight through the optic without reflecting off any surface and reached the detector.

The GR component is axisymmetric along the line from the source to the OA. The primary concern is that photons from a distant source will interfere with the analysis of a focused target source, but, as shown, there are often free regions on the detector, and ultimately it is the relative strengths and relative location of the two sources that decide whether the GR becomes a significant issue.

Because of the nonuniformity, it is not practical to calculate the GR flux with respect to a typical extraction region. Instead, we show in Fig. 6 the spectrum of the GR, including the reflectivity component, as collected from the entire detector as a fraction of the source spectrum had it been imaged on-axis. Below 10 keV, the effective area remains close to the geometrical area due to the fact that most shells have grazing incidence angles less than the critical angle. The critical angle is the angle below which x-rays undergo total external reflection. For angles less than the critical, the reflectivity is, therefore, close to 100% and the majority of photons are successfully reflected. This is seen as a flat spectrum, with only a very slight energy dependency, because the critical angle changes across the shells. Above 10 keV, reflection alters the spectrum of the GR. The inner shells, responsible for most of the high-energy area, are rejected

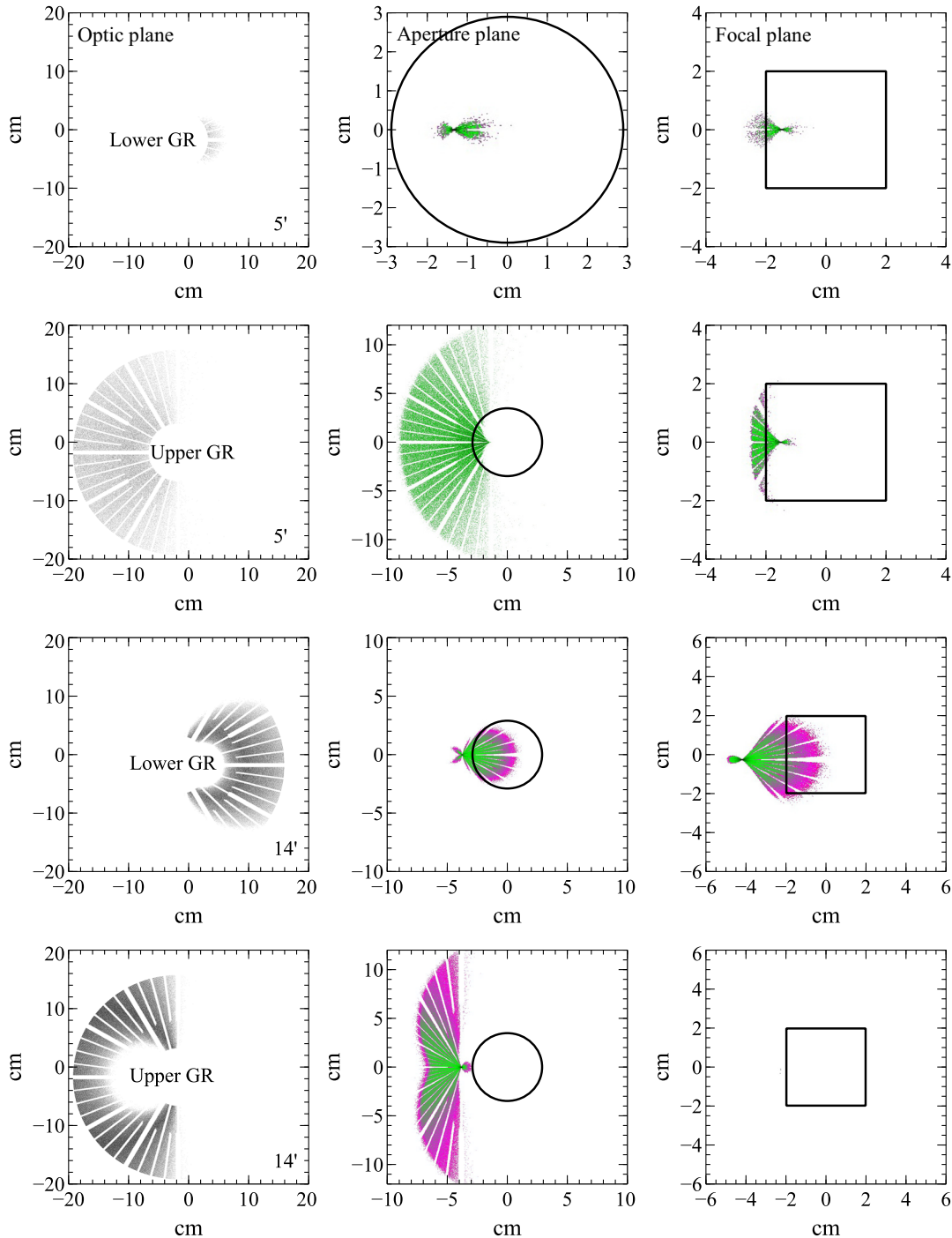


Fig. 4 The photon path of the upper and lower GR component from a source at 5' and 14' shown right after the photons have exited the optics (optic plane), at the location of the limiting aperture (aperture plane), and finally at the focal plane, for which we have removed all aperture stop rejected photons. The circle shows the extent of the aperture stop opening and any photons outside will be rejected. The square shows the extent of the focal plane detectors. Physically, the source is moving along the positive x -axis, while its image is moving along the negative x -axis.

by the aperture stop with increasing off-axis angles (see Fig. 4)—and conversely the outer shells responsible for most of the mid-range energy throughput are rejected by the aperture stop at smaller angles—which is why in Fig. 6 there is first an increase in the high-energy part of the spectrum and then a decrease at higher off-axis angles.

3.1 Effective Area Corrections

As demonstrated above, the GR component appears as early as 2' off-axis but only becomes significant above 3'. In most cases, planned science targets are located within 2' of the OA, but that is not always the case. In these instances, a source may

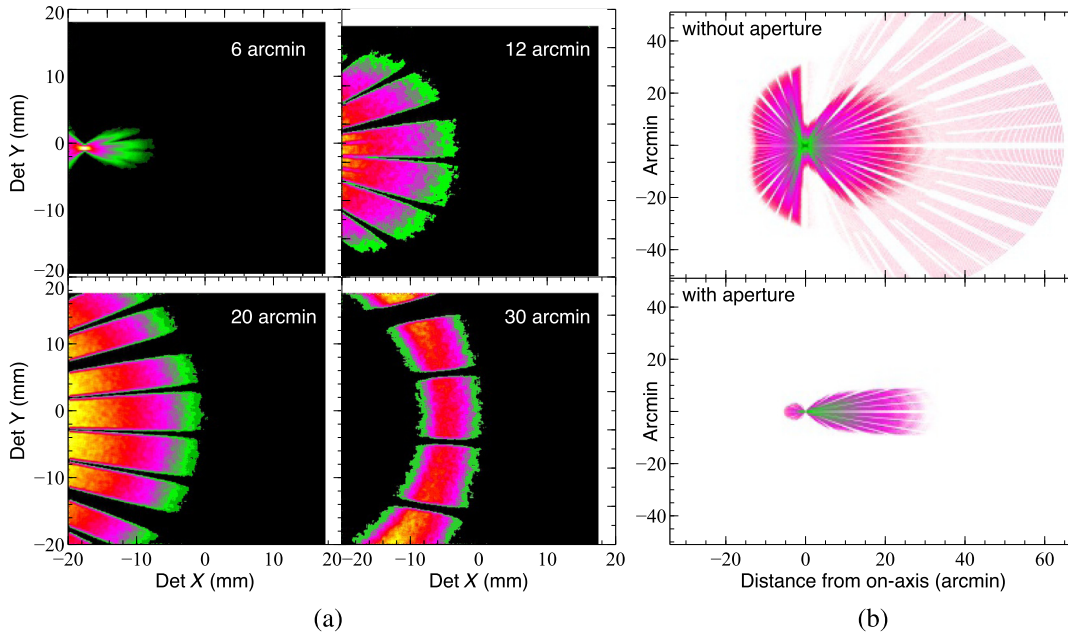


Fig. 5 (a) Ray-trace simulation of GR falling on the detectors at different off-axis angles. (b) Composite image of the GR pattern from a source for every 2' for an infinite focal plane. Photons that slip straight through the optics without reflecting on either surface can be seen extending like a fan from 20' to 60'. These and a large part of the GR are rejected by the aperture stop.

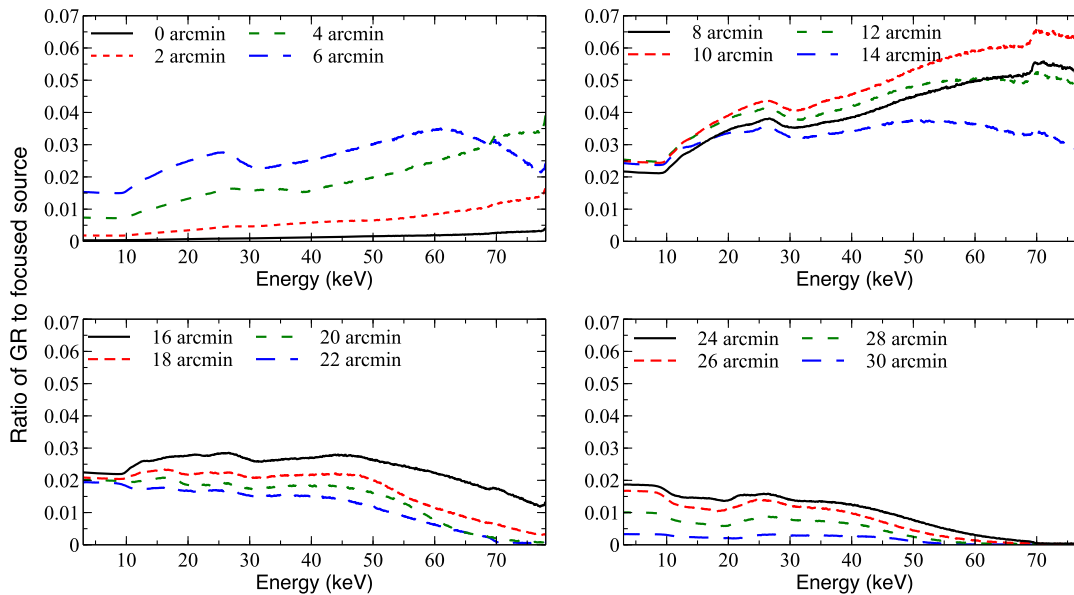


Fig. 6 Ratio of the total number of GR photons falling on the detector to the total number of source photons collected at the focal plane from its on-axis position. In this raytrace, the reflectivity component has been included. As shown in Fig. 5, the GR illumination is not uniform across the detector, and these curves are, therefore, not representative of an area average but of the total spectrum collected from the entire focal plane. The curves show that small off-axis angles are dominated by the inner shells, which are predominantly responsible for the high-energy throughput, while with increasing off-axis angles the low energy, outer shells dominate.

contaminate itself with its own GR. This leads to an increase in the source spectrum, and, because of the nonuniform nature of the GR, it is not practical to treat it as an additional background. Instead, we have modified the effective area to properly account for the GR inclusions.

While the GR increases the area, the aperture stop, responsible for reducing the diffuse background by limiting the FoV,

also decreases the area with increasing off-axis angles due to the clipping of the edges of the optical path between detector and optic. This is primarily a geometrical effect, but, because each reflecting shell has a different energy response, the selective rejection of different shells introduces a spectral dependency for both the aperture and the GR component, which is also subjected to the aperture correction.

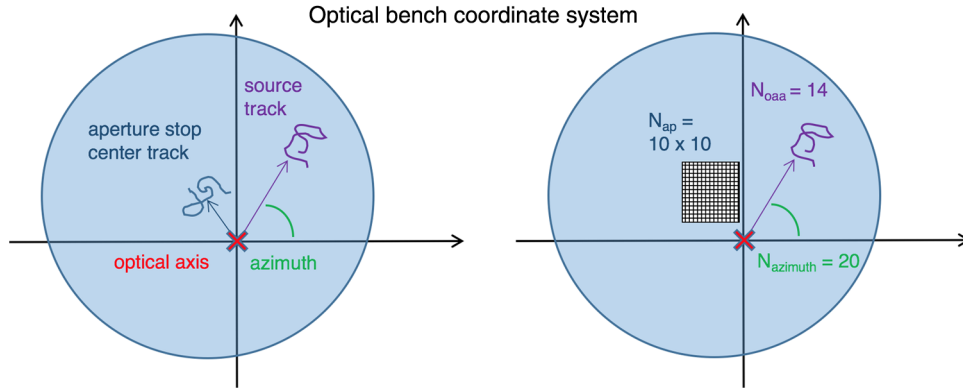


Fig. 7 GR and aperture stop correction schematic. The optics and their OA are stationary in the optical bench coordinate system. The circle represents the aperture stop and as a function of time we keep track of the center of the aperture with respect to the optics. The source moves along a different path caused by the spacecraft jitter. To cover all motions, we raytrace 20 azimuth angles for every 18 deg, 14 off-axis angles binned every arcminute, and 10×10 aperture stop positions at 1-mm resolution.

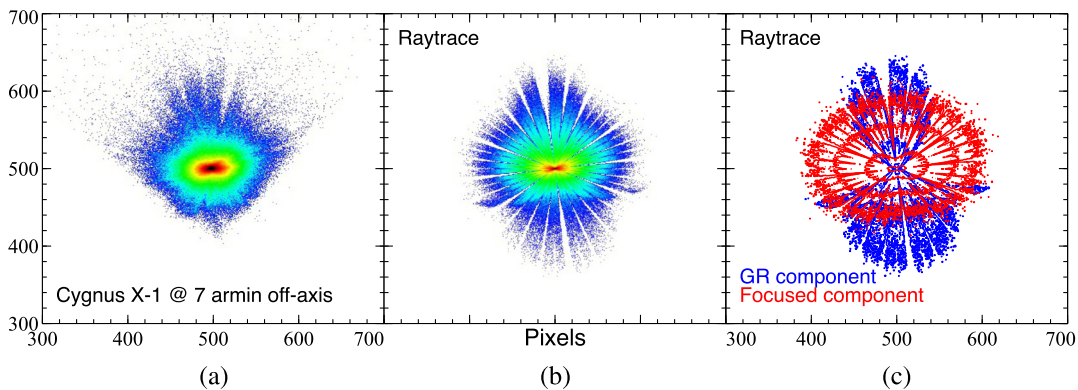


Fig. 8 (a) Off-axis observation of Cygnus X-1 (NuSTAR observation ID: 10014001001). The sharp edges at the bottom are the detector edges. (b) Raytrace of the Cygnus X-1 observation. Detector extent not included. (c) Contours of the raytraced image are shown decomposed into the focused source component (properly double bounced photons) and the GR component to illustrate how different extraction regions centered on the source sample different amounts of the GR.

To complicate matters further, thermal gradients along the mast cause it to flex on an orbital time scale,⁴ and the motion smears out the PSF on the detector plane, resulting in a time-dependent clipping of the area. However, the problem is completely determined by knowing the relative location of the aperture stop, stationary with respect to the detectors, and the focal plane bench, with respect to the OA location, stationary in the optical bench frame. The two benches relative motions are tracked and reconstructed by a laser metrology system.³ Figure 7 lays out the geometry and time-dependent terms. The coordinate frame is set in the optical bench frame since this is where the OA is stationary. The circle represents the aperture stop, and the blue track is the motion of its center to the frame. The source, shown as the purple track, will follow its own motion based on the combined spacecraft jitter and mast motion. Because the aperture stop is not centered on the source, it is necessary to take the azimuth into account as well.

To generate the corrections, we ran raytraces that covered a phase space of 20 azimuth angles for every 18 deg, 14 off-axis angles binned every arcminute, and 10×10 aperture stop positions at 1-mm resolution. We assumed a fixed PSF size for all energies with scattering parameters inside the

raytrace adjusted to reproduce the observed polychromatic Hercules X-1 PSF. Thus, we did not take into account the secondary term of the PSF varying in size as a function of energy.¹¹

The above terms all go into calculating the aperture stop correction, but, in addition to these, the GR correction also requires the specification of an extraction region. This necessity is illustrated in Fig. 8 where we have shown an off-axis observation of the bright accreting black hole x-ray binary Cygnus X-1 (a), the raytraced observation (b), and the same raytrace where we have separated the focused photons from the GR component (c). The amount that the GR component contributes is dependent on the size of the extraction region, and, due to the obvious complexity of the GR pattern, the corrections were only derived for circular regions, which we include in steps of $20''$ in radius.

An example of the magnitude of the aperture and GR corrections is shown in Fig. 9. The aperture correction is less than unity because it is removing photons from the effective area, and it is largest for low-energy photons since the majority of these come from the outer shells of the optic and thus are more prone to being blocked by the aperture than light focused by the inner shells. The correction is only important for off-axis angles $> 3'$. For the GR corrections, the net effect is an increased

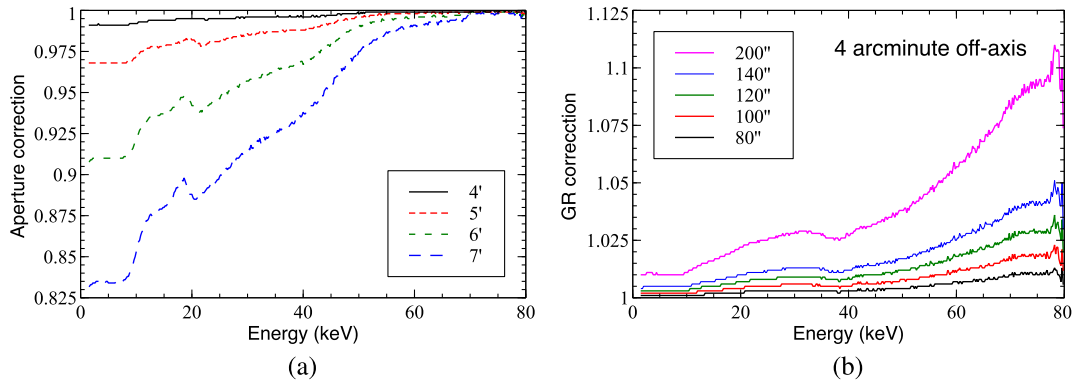


Fig. 9 (a) Correction to the effective area of proper double bounced photons due to the aperture stop. (b) Correction to the effective area due to the inclusion of GR photons for different extraction region sizes. The GR-correction also contains aperture corrections of the GR photons.

effective area. The suppression of the low energies is because of the aperture stop correction to the GR. Both corrections are of a linear nature as a function of the off-axis angle, and, in practice, we interpolate the correction tables when generating the observation specific instrument response.

3.2 The “Streak”

The “streak” is an artifact that is rare because it requires a fairly exact alignment of the source to the optics and detectors. It is caused by the absence of glass between mirror segments as shown in Fig. 2(b), which allows the photons to pass right through the optics without reflecting off any surface and propagate down to the focal plane. This gap occurs at 60-deg intervals, and, to reach the focal plane, the source must be aligned azimuthally with one of the gaps and be within the correct off-axis

angle. Since there are no gaps between shells with a radius smaller than the intermediate mandrel, the smallest angle at which a photon can make it through to the focal plane is given by the radius of the intermediate mandrel at an $R \sim 108.7$ mm (shell 69), $\theta_{\min} \sim 37'$. The largest angle is determined by the size of the optics and is $\theta_{\max} \sim 65'$.

These streaks are rare, but they have been observed at several locations in the Galactic Center. They were caused by the same source, and, once the full mosaic was compiled, as shown in Fig. 10, they were identified as originating from the binary 1A 1743-294 in an outburst during the observations.¹²

3.3 Back Reflections

In BR, the photons strike the backside of the upper mirror of the adjacent shell first then reflect again off the front side of

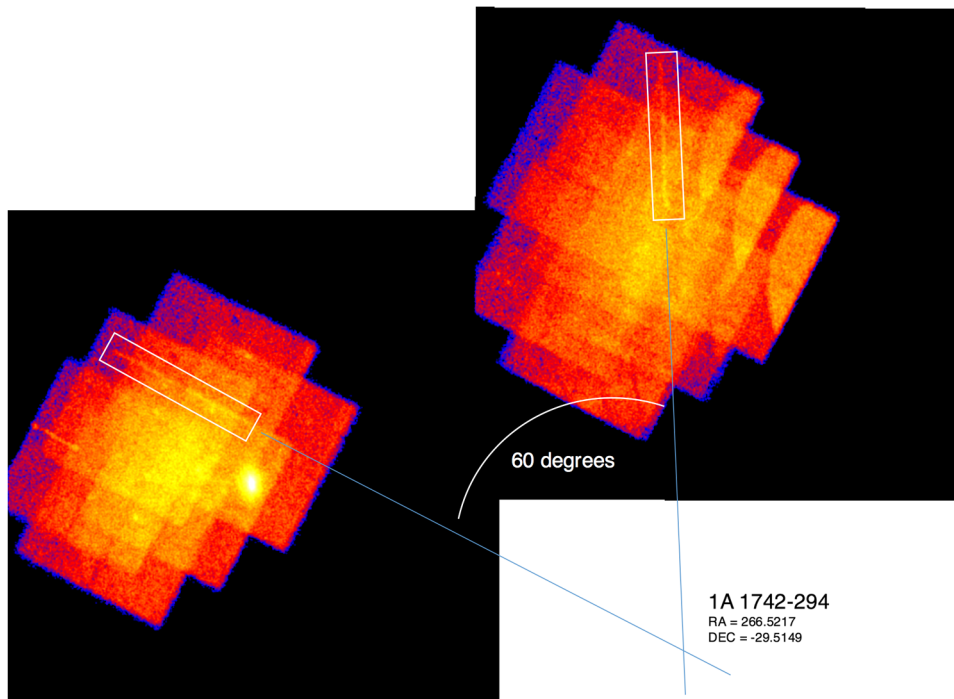


Fig. 10 During a Galactic Plane survey,¹² the streak appeared at two different locations, and, by generating the sky mosaic and tracing back the streaks, it was discovered that they came from 1A 1742-294, an x-ray binary that was in outburst.

the mirror shell. Because the graze angles of adjacent shells are only slightly different, the photons exit at almost the same angle at which they came from the source.

Like for the GR, the BR is limited to certain off-axis angles, and at any particular off-axis angle only a few shells contribute at a time. As shown in Fig. 3, the condition for a photon to exit the optics is constrained by the opening angle of the lower shell. For the innermost shell, the allowed angles are $\sim 14 \pm 9'$, and for the outermost shell it is $\sim 24 \pm 24'$. The aperture stop further limits these angles, and the geometrical area obtained without including the reflection is shown in Fig. 3.

Reflection from the backside requires very high fluxes to be detected and cannot be seen from typical astrophysical sources. This component was, however, observed during the solar observations on 11 October 2014 when a solar X-class flare went off a few hours before the scheduled observations. We show in Fig. 11 an example of how the component looks with the accompanying raytrace simulation (a), the full mosaic of the actual observation (b), and its raytrace (c). The slew was away from the solar north pole, and the bright streak is the flare entering in through the mirror gap. In the simulations, the mirror gap is larger than in reality; we simulated the as-designed width of the double street, spacer to spacer (see Fig. 2), which assumes that the mirror overhang between the spacers is nonfocusing due to the surface not being constrained to a conical shape anymore. From imaging data, there is some indication that at least part of the mirror overhang is properly focusing, but, taken together with the jagged edges of the glass, we have no good way of estimating how much that is. The sharp circular edges are caused by the aperture stop. In the bottom of the mosaic, the GR component is just visible as a brighter area before transitioning to the BR. We ran the simulation with a longer exposure time than the actual observation to get better fidelity and more detail in the transition area between GR and BR and to reduce the errors on the effective area calculation.

To estimate the true effective area of this component, we require knowledge of the reflectivity coefficients off the backside of the mirror. We calculated the reflectivity from the inverted multilayer stack with an added 0.21-mm SiO_2 substrate at the top and found that very few photons make it into the stack through the substrate at the angles in question, making the glass substrate the primary contributor. Because of the inefficiency of SiO_2 as a reflective surface, only soft photons that can undergo total external reflection have a nonnegligible contribution. This causes the BR component to cut-off sharply between 3 and 5 keV as shown in Fig. 12(a). The mean effective area between 3 and 5 keV [black curve in Fig. 12(b)] is obtained from the raytrace using the mean SiO_2 reflectivities between 3 and 5 keV for the first reflection and the NuSTAR multilayer recipes⁹ for the second reflection. We did not include the optics thermal cover and detector window Be absorption, and the area has been scaled to the photons falling on the detector area only.

To obtain an independent verification of the effective area, we studied the full mosaic of the solar observation. Thanks to the streak, we can extract a flux for the solar flare for the tiles where it was present. The solar flux is extracted from the detector by laying down an area around the streak and using that as the effective area, including all absorption effects in the photon path.¹³ We then extracted the photon count from the remaining detector, limiting the energy range to be between 3 and 5 keV. The effective area is obtained by dividing the detector photon rate with the expected flux and as shown in Fig. 12(b) there is good agreement between the two estimates.

The errors on the effective area from the observation mainly come from evaluating the area of the streak, which is almost certainly narrower than the extraction region laid down on the detector. The jagged edges of the mirror also vary the gap width and cause additional scattering; thus, we estimate a 50% error on the area. On the raytrace side, we assumed the mean reflection values between 3 and 5 keV for the backside of the mirrors

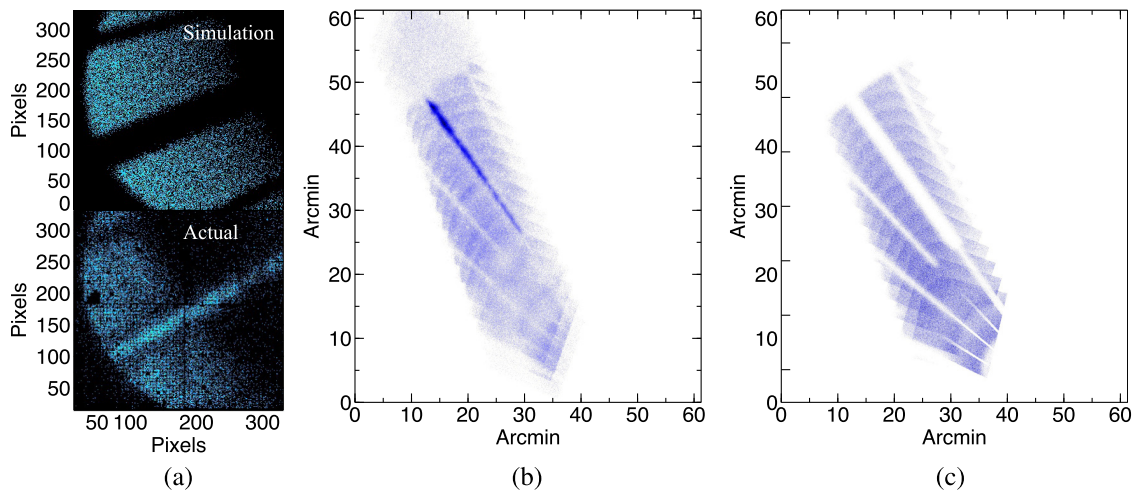


Fig. 11 (a) Two examples of the GR and BR distribution on the detector from actual NuSTAR data and simulation. The fidelity of the simulation is greater than for the actual since the detectors were operating at 99% dead-time with practical exposure times on the order of ~ 20 s. (b) Solar observation, north pole slew. The additional counts apparent at y -axis 50 to 60" are from the diffuse cosmic x-ray background. (c) Raytrace of the same observation. The narrow stripes show where the spacers are blocking the x-rays. The broad stripe has no mirror, and we see photons in the actual observation at that location because it happens to be centered such that the flux from the solar x-flare is allowed to pass through. In the bottom of (c), the first 10' are GR.

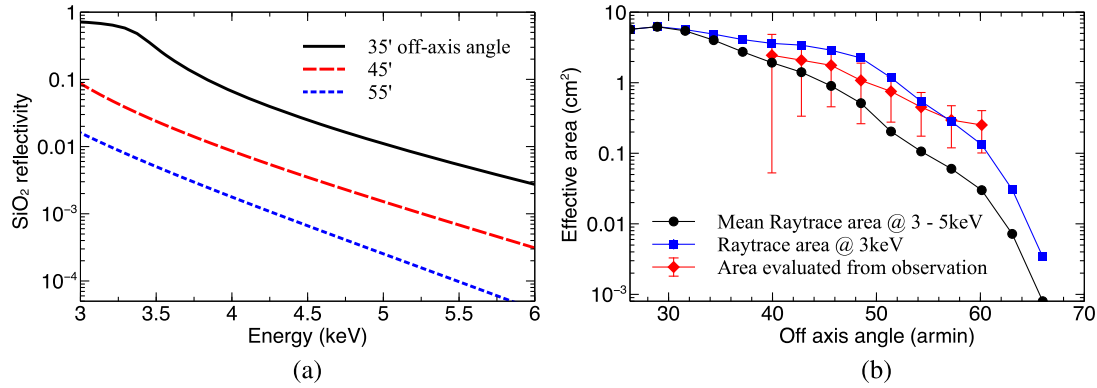


Fig. 12 (a) The reflectivity curves of a photon reflecting off a 0.21 mm SiO_2 substrate at three different grazing incidence angles. (b) The average effective area between 3 and 5 keV for the detector from the raytrace assuming averaged reflection coefficients and effective area obtained from the actual NuSTAR observation of the sun.

without weighting it by an input spectrum. This will underestimate the area at higher off-axis angles due to there being more low-energy than high-energy photons in the averaged energy interval. In comparison, we show the raytrace effective area at 3 keV, which as expected shows better agreement with the measured area.

In comparison, the on-axis effective area in the same energy band is $\sim 500 \text{ cm}^2$ focused on a small area instead of the entire detector. If we take the typical extraction area to be the PSF half power diameter, which is $1'$ or 2.9 mm, then the area of the extraction region is 6.6 mm^2 and the effective area per detector area is $\sim 500/6.6 = 75 \text{ cm}^2 \text{ mm}^{-2}$. The BR flux covers on average about 70% of the detector area, which is 1120 mm^2 , so the effective area per detector area for 1 cm^2 of BR is $\sim 1 \times 10^{-3} \text{ cm}^2 \text{ mm}^{-2}$. The source count rate is thus reduced by a factor of $\sim 7.5 \times 10^4$ in a comparable typical extraction region and thus is completely negligible if caused by typical astrophysical sources.

4 Stray Light

4.1 Primary Stray Light

SL is the term given to photons that arrive directly at the focal plane without having undergone any reflection or transmission through the optics.

The geometry of the SL is determined by the aperture stops, Fig. 1(b), and the silhouette of the optical bench. A schematic of the optical bench is shown in Fig. 13 and outlines the angular extent of the bench as seen from the detectors. The circle marks the FoV of the sky as seen from the center of one detector up through the aperture stop. Within this FoV, there are slices of sky that are not blocked by either the aperture or the bench, and if a source should be located there it may directly reach the focal plane. If a source does happen to occupy that space, it can be blocked by choosing a different position angle (PA) of the observatory, which rotates the outline of the bench on the sky. Different areas of the detector see different areas of the

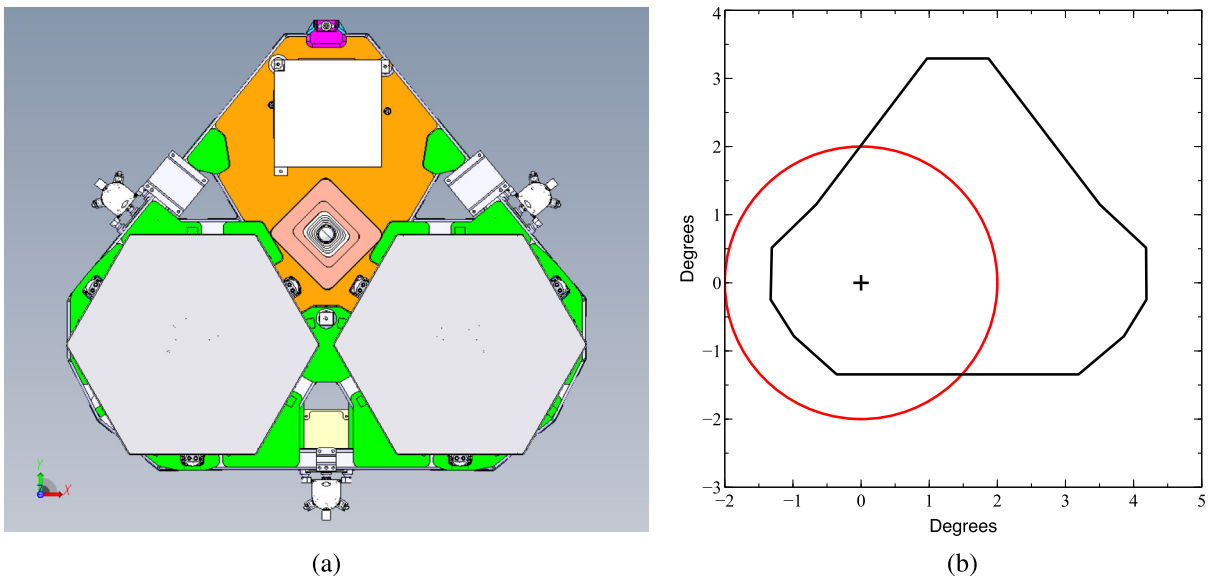


Fig. 13 (a) The OB as seen from the sky. Hexagonal plates mark the location of the two optics. (b) Projected outline of the OB in degrees on the sky as seen from the detectors. Red circle is the projected opening of the limiting aperture stop for the center of one of the modules. This circle is displaced depending where on the detector one is looking up from, with a max displacement of 2 deg.

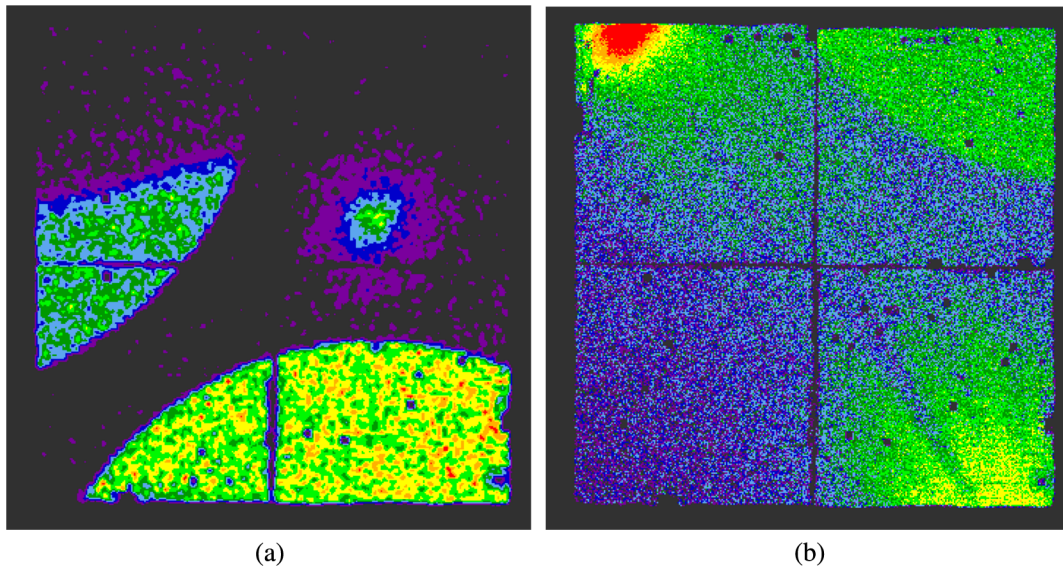


Fig. 14 (a) SL pattern in NuSTAR observation obsID: 90201027002. The source can be seen in the top right quadrant. The truncation of one crescent is the optical bench blocking the photons. The PA was chosen to allow the source to fall in a SL-free region. The image has been smoothed with a 3 pixel Gaussian. (b) Example of NuSTAR observation obsID: 90201020002 that has both GR and SL.

sky, and SL may occur from sources within 1 deg to 4 deg of the observed target.

This component places by far the tightest constraints on the planning of observations. The SL can, in most cases, be completely avoided by picking a suitable PA, but this in turn limits the times a year a target can be observed. Figure 14(a) shows an example of careful planning that enables a source to be observed despite multiple SL sources. We also show an example in Fig. 14(b) where both SL and GR were present to illustrate the visual difference between the two components. The characteristic circular shape of the SL comes from the aperture stop, and, because of the simple geometry, it is straightforward to predict the location of the SL.

In the rare instances that a science target cannot be scheduled to avoid SL, the SL needs to be treated as an additional background. Fortunately, there are a couple of mitigating factors that make analysis straightforward.

- Within the illuminated area, the spectrum is constant as a function of location. Obtaining a spectrum just requires replacing the mirror effective area with the area covered by the detector. Details on the exact method can be found in Ref. 13.
- Background subtraction is often the greatest concern when dealing with SL. However, due to the unfocused nature of the SL and the typically exponentially declining spectra, the SL spectrum has often fallen far below the internal background at energies where background matters and, therefore, sometimes can be ignored altogether.

With careful analysis, most SL regions can, therefore, be dealt with even if they overlap the actual target of the observation.

4.2 Absorbed Stray Light

Similar to the primary SL, absorbed stray light (ASL) also arrives at the focal plane directly from the source, but the angles

are larger, going all the way out to 10 deg, and they do so by transmission through the material of the aperture stops.

The aperture stops were designed to be 1.88 mm, layered into 0.75 mm Al, 0.13 mm Cu, and 1.0 mm Sn. However, as we will show below, they appear to have been built without the 1.0 mm Sn. This allows strong hard spectral sources to transmit through the apertures above ~ 20 keV. Unlike the primary unabsorbed SL, this component is very weak and only a handful of the brightest astrophysical sources (e.g., the Crab, Cygnus X-1, and GX 9+9) have been capable of producing a significant detection. Over five years of operation, less than ten observations have been impacted.

Figure 15 shows a schematic of the geometry. The top is the limiting aperture, and it leaves a circular SL as illustrated in shade. For strong sources, the high-energy flux is capable of transmission through the aperture stop and thus photons that have progressed through the first aperture stop and managed to slip through the opening of the second, leave another circle, or crescent, of once absorbed photons. Photons that have transmitted through the first and the second aperture stop material leave a third circle of twice absorbed photons. The top of the detector module is a square opening (“the can”) that only allows photons to pass through the opening; there is no transmission from photons that hit the side. Any photons arriving at angles that are larger than the can’s FoV are rejected. Due to their complexity [Fig. 1(b)], we do not model the fixtures that hold the apertures in place, and observations have shown that we can ignore its extent since the “can” excludes photons that arrive at angles where absorption from the fixture would have been important. Note, however, that a photon may transmit through AP2 or AP3 without having encountered AP1 or AP2.

Figure 16 shows the predicted ASL from Cygnus X-1 at an off-axis angle of 3.98 deg (a) and the actual detector image of the observation (b). It is easy to see that there is additional flux on the detectors, but, without the predictive plots, distinguishing the boundaries is not straightforward. The flux is, therefore, not even across the ASL region the way it is for the primary SL, and treating it as an additional background is difficult without

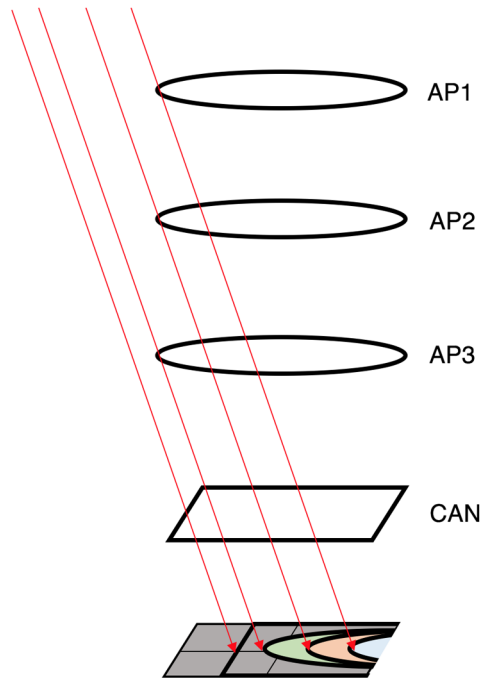


Fig. 15 Aperture stop schematic. There are three aperture stops, surrounded by 0.13 mm Cu and 0.75 mm Al, and a square opening in the detector module acting as the fourth. Rays that enter through the top aperture and hit the detector without transmitting through any of the other apertures is the primary SL (blue circle). Rays that transmit through the first aperture are single absorbed (orange circle), and rays that transmit through the first and second aperture stop are double absorbed (green circle).

precise knowledge of both the actual source spectrum, the layout of the absorbing elements, and their relative occupation underneath the target source.

The ASL spectrum itself can be easily identified because of its characteristic low-energy absorption and peak flux at 20 to 40 keV. Figure 17(b) shows the Crab spectrum as extracted from the single absorbed and double absorbed regions (a). We also extracted the Crab spectrum from the SL region and applied to it the absorption from single and twice absorbed 0.75 mm Al and 0.13 mm Cu. This unfortunately shows the absence of the Sn, which would have completely suppressed the spectrum had it been present.

Because of the complicated patterns, albeit predictable, the ASL currently requires specialized, nonstandard treatment.

5 Summary and Discussion

We summarize in Table 1 the different components and the approximate off-axis locations for where they may be observed. All of these artifacts are predictable and most could have been avoided altogether as we will discuss below. We, therefore, strongly encourage future observatories to investigate each of these components in their optical design.

The GR are the most difficult to design against. In this paper, we used the raytrace approach to investigate the GR and BR because we knew the precise geometrical layout of our instrument and the optical prescription of the multilayer recipes. However, in the concept designs where a phase-space is being considered, there are excellent analytic approaches to help in such an investigation.^{14,15} Some reduction of these components can be achieved by changing the shell spacing and

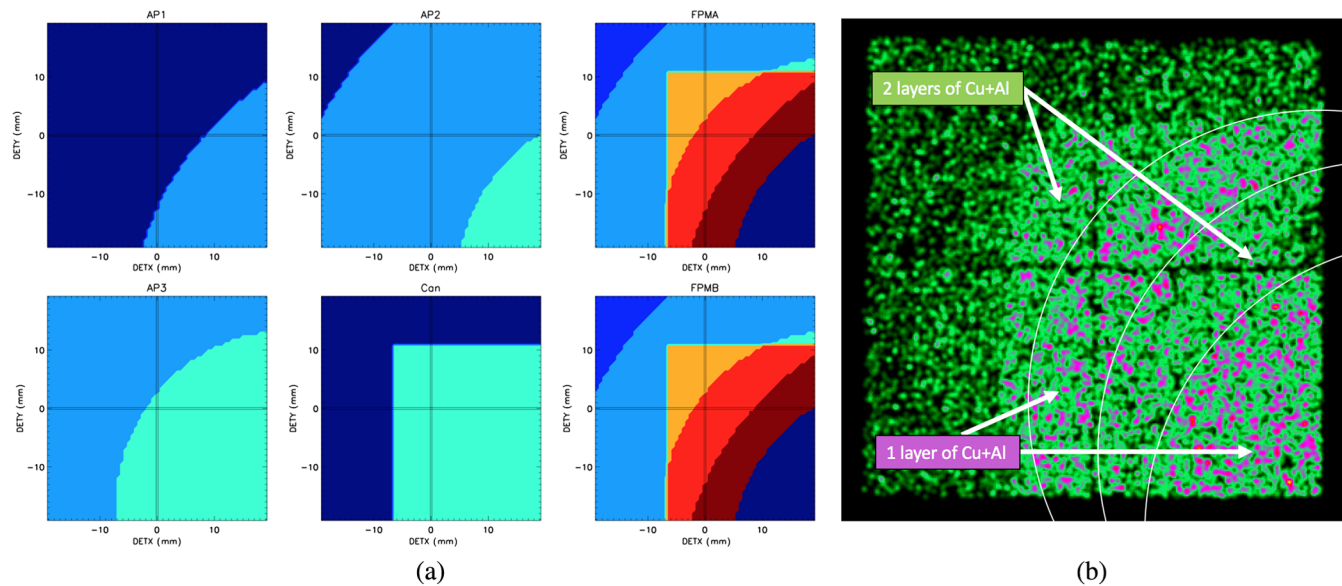


Fig. 16 (a) Predicted ASL. The four aperture plots individually show the projection of each aperture (AP1-3) and the “can,” and the two plots labeled “FPMA” and “FPMB” are the summed aperture images on the two modules (for certain angles, the two can be different). In these two latter plots, the color shading is a visual aid to distinguish the different regions and should not be taken literally. In the four aperture plots, the smallest (lightest shade, green) crescent shows where SL passes through unabsorbed, and the second largest circle (light blue) where it is absorbed by a single layer of Cu + Al. The darkest region (dark blue) represents the fixture, which we do not model due to its complexity, and observations show that we can ignore its extent since the “can” excludes photons that arrive at angles where the fixture would have been important, like in this example. (b) Actual ASL. Without the predicted ASL pattern it would be difficult to see where it is once and twice absorbed.

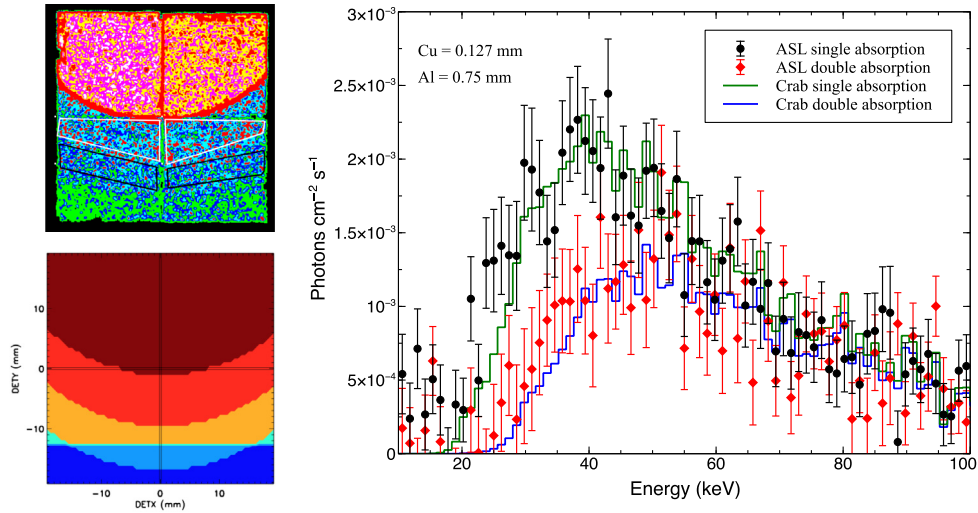


Fig. 17 (a) Actual and predicted ASL pattern for Crab observation (NuSTAR observation ID: 1011005001) positioned 1.9-deg off-axis. The white regions are of single absorbed and black regions are of double absorbed. (b) The spectra of the single absorbed and double absorbed regions together with the Crab SL spectrum from the top of the detector with the as-built absorption of Cu and Al applied.

Table 1 Summary of artifacts.

Component	Minimum angle	Maximum angle
GR upper reflection (°)	2	10
GR lower reflection (°)	5	30
BR (°)	15	65
Streak (°)	37	65
SL (deg)	1	4
ASL (deg)	1	10

length of the mirrors, but as mentioned it cannot completely eliminate the GR. To further reduce the GR, baffling of some sort is required. For NuSTAR, we designed a baffle made of Invar to be placed in front of the optics that extended the height of the mirror shells to reject photons coming in at a range of off-axis angles. However, due to launch mass constraints, it was not implemented. A similar design was used for XMM-Newton and with it they are able to reduce about 80% of the GR flux.¹⁶ When the shell spacing is larger, as it is for Chandra, the baffling can be done within the optics.^{17,18}

To reduce the SL and background, NuSTAR designed a deployable optical shield, which would have increased the angular extent of the optical bench; although built, it was never mounted due to prelaunch scheduling constraints. An alternative approach for soft x-ray instruments would be to shroud the optical path, but in the case of NuSTAR that was not a feasible approach since the amount of shielding required to stop the high-energy flux would have been prohibitive. For future hard x-ray instrumentation with long focal lengths, careful thought must, therefore, be put into the design of baffling and apertures down the length of the optical path.

For the ASL, the inclusion of Sn in the apertures as designed would have been sufficient to eliminate the component.

Elimination of the “streak” could have been achieved simply by blocking the gap between mirror segments.

Overall, the artifacts have resulted in some scheduling constraints for the planning of targets. Because of the GR, there is a region around bright sources ($<1'$) where a target of an observation must be of a certain brightness to not be affected by GR. Even then, as demonstrated, the GR often leaves contamination free regions. When allowing for different observing angles, and waiting out the contamination of bright transients, the majority of targets can be observed without significant issues.

Acknowledgments

This work was supported under NASA Contract No. NNG08FD60C and made use of data from the NuSTAR mission, a project led by the California Institute of Technology, managed by the Jet Propulsion Laboratory, and funded by the National Aeronautics and Space Administration. We thank the NuSTAR Operations, Software, and Calibration teams for support with the execution and analysis of these observations. This research has made use of the NuSTAR Data Analysis Software (NuSTARDAS) jointly developed by the ASI Science Data Center (ASDC, Italy) and the California Institute of Technology.

References

1. F. A. Harrison et al., “The Nuclear Spectroscopic Telescope Array (NuSTAR) high-energy x-ray mission,” *Astrophys. J.* **770**, 103 (2013).
2. R. Petre and P. Serlemitsos, “Conical imaging mirrors for high-speed x-ray telescopes,” *Appl. Opt.* **24**, 1833–1837 (1985).
3. D. I. Harp et al., “NuSTAR: system engineering and modeling challenges in pointing reconstruction for a deployable x-ray telescope,” *Proc. SPIE* **7738**, 77380Z (2010).
4. K. Forster et al., “Getting NuSTAR on target: predicting mast motion,” *Proc. SPIE* **9910**, 99100Z (2016).
5. H. Wolter, “Spiegelsysteme streifenden einfalls als abbildende optiken für röntgenstrahlen,” *Ann. Phys.* **445**, 94–114 (1952).
6. H. Wolter, “Verallgemeinerte schwarzchildsche spiegelsysteme streifender reflexion als optiken für röntgenstrahlen,” *Ann. Phys.* **445**, 286–295 (1952).
7. D. R. Wik et al., “NuSTAR Observations of the bullet cluster: constraints on inverse compton emission,” *Astrophys. J.* **792**, 48 (2014).

8. K. D. Joensen et al., "Design of grazing-incidence multilayer supermirrors for hard-x-ray reflectors," *Appl. Opt.* **34**, 7935–7944 (1995).
9. K. K. Madsen et al., "Optimizations of Pt/SiC and W/Si multilayers for the Nuclear Spectroscopic Telescope Array," *Proc. SPIE* **7437**, 743716 (2009).
10. W. W. Craig et al., "Fabrication of the NuSTAR flight optics," *Proc. SPIE* **8147**, 81470H (2011).
11. H. An et al., "In-flight PSF calibration of the NuSTAR hard x-ray optics," *Proc. SPIE* **9144**, 91441Q (2014).
12. J. Hong et al., "NuSTAR hard x-ray survey of the galactic center region. II. X-ray point sources," *Astrophys. J.* **825**, 132 (2016).
13. K. K. Madsen et al., "Measurement of the absolute crab flux with NuSTAR," *Astrophys. J.* **841**, 56 (2017).
14. D. Spiga, "Optics for x-ray telescopes: analytical treatment of the off-axis effective area of mirrors in optical modules," *Astron. Astrophys.* **529**, A18 (2011).
15. D. Spiga, "Analytical computation of stray light in nested mirror modules for x-ray telescopes," *Proc. SPIE* **9603**, 96030H (2016).
16. D. de Chambure et al., "X-ray baffle of the XMM telescope: development and results," *Proc. SPIE* **3737**, 396–408 (1999).
17. T. J. Gaetz et al., "Orbital verification of the CXO high-resolution mirror assembly alignment and vignetting," *Proc. SPIE* **4012**, 41–52 (2000).
18. G. Cusumano et al., "Simbol-X: x-ray baffle for stray-light reduction," *Proc. SPIE* **6688**, 66880C (2007).

Kristin K. Madsen received her PhD in astrophysics from the University of Copenhagen in 2007. She has more than 10 years of experience in x-ray optics and astrophysical research and is currently a staff scientist at California Institute of Technology as one of the principle instrument and mission scientists for NuSTAR. Her research interests include active galactic nuclei, x-ray binaries, pulsar wind nebulae, and hard x-ray optical design.

Finn E. Christensen received his PhD from the Danish Technical University in 1982. He is currently is a senior staff scientist at DTU-space, and he has more than 30 years of experience in developing, studying, and calibrating x-ray optics for space research. His current research revolves around developing and calibrating the coatings for the ATHENA mission.

William W. Craig received his PhD in astrophysics from U.C. Berkeley in 1994. He has more than 20 years of experience in

astrophysical instrumentation and research, working with both optical and detector systems, and has worked on numerous space missions including XMM-Newton, CHIPS, GLAST, NuSTAR, and ICON, as well as a number of balloon-borne instruments. He is currently the project manager for the Ionospheric Connections Explorer (ICON) at UC Berkeley.

Karl W. Forster is a graduate of the University of Leicester and the University of Hertfordshire, UK, and received his PhD in astronomy from Columbia University. His research interest includes high-energy emission from active galactic nuclei, and he has developed and managed science operations for NASA missions GALEX and NuSTAR.

Brian W. Grefenstette is a research scientist at the California Institute of Technology. He is one of the principle mission scientists for NuSTAR, working on the calibration of the focal plane detectors. His science interests include nuclear astrophysics, x-ray binaries, supernovae, and supernova remnants.

Fiona A. Harrison received her PhD in physics from the University of California, Berkeley, in 1993. She is the California Institute of Technology (Caltech) Benjamin M. Rosen Professor of Physics and the Kent and Joyce Kresa Leadership Chair of the Division of Physics, Mathematics, and Astronomy. Her research is focused on the study of energetic phenomena ranging from gamma-ray bursts and black holes on all mass scales to neutron stars and supernovae. She is the principal investigator for NuSTAR.

Hiromasa Miyasaka received his PhD in physics from Saitama University, Japan, in 2000. He has worked on numerous space missions, including French-Brazilian microsatellite, Suzaku, STEREO, NuSTAR, and Parker Solar Probe. He is involved in the development of various radiation detectors as well as custom low-noise application specific integrated circuits (ASIC). He is currently a staff member of NuSTAR Science Operation Center at Caltech.

Vikram Rana received his PhD in astronomy and astrophysics from Tata Institute of Fundamental Research (TIFR), India, in 2006. He is a staff scientist in the Space Radiation Laboratory at Caltech. His research experience includes the development of x-ray optics for Astrosat and focal plane radiation detectors for NuSTAR missions. He is also interested in studying x-ray emissions from ultraluminous x-ray sources, x-ray binaries, and cataclysmic variables.